Temperature-driven reorganization of electronic order in CsV_3Sb_5

Q. Stahl,[1] D. Chen,[2] T. Ritschel,[1] C. Shekhar,[2] E. Sadrollahi,[1] M. C. Rahn,[1] O. Ivashko,[3] M. v. Zimmermann,[3] C. Felser,[2,4] and J. Geck[1,4,*]

[1]*Institute of Solid State and Materials Physics, TU Dresden, 01069 Dresden, Germany*
[2]*Max Planck Institute for Chemical Physics of Solids, Dresden, Germany*
[3]*Deutsches Elektronensynchrotron DESY, Notkestrasse 85, 22603 Hamburg, Germany*
[4]*Würzburg-Dresden Cluster of Excellence ct.qmat, Technische Universität Dresden, 01062 Dresden, Germany*

(Received 5 December 2021; accepted 4 May 2022; published 24 May 2022)

We report x-ray diffraction studies of the electronic ordering instabilities in the kagome material CsV_3Sb_5 as a function of temperature and applied magnetic field. Our zero-field measurements between 10 and 120 K reveal an unexpected reorganization of the three-dimensional electronic order in the bulk of CsV_3Sb_5: At low temperatures, a $2\times2\times2$ superstructure modulation due to electronic order is observed, which upon warming changes to a $2\times2\times4$ superstructure at 60 K. The electronic order-order transition discovered here involves a change in the stacking of electronically ordered V_3Sb_5 layers, which coincides with anomalies previously observed in magnetotransport measurements. This implies that the temperature-dependent three-dimensional electronic order plays a decisive role for transport properties, which are related to the Berry curvature of the V bands. We also show that the bulk electronic order in CsV_3Sb_5 breaks the sixfold rotational symmetry of the underlying $P6/mmm$ lattice and perform a crystallographic analysis of the $2\times2\times2$ phase. The latter yields two possible superlattices, namely a staggered star-of-David and a staggered inverse star-of-David structure. Applied magnetic fields up to 10 T have no effect on the x-ray diffraction signal. This, however, does not rule out time-reversal symmetry breaking in CsV_3Sb_5.

DOI: 10.1103/PhysRevB.105.195136

I. INTRODUCTION

The physics of quantum materials containing layers of corner-sharing triangles is full of surprises. Not only that localized magnetic moments on kagome lattices provide a unique platform for novel magnetic states of matter [1]. As it is now becoming more and more evident, also delocalized electrons on a kagome lattice can exhibit novel and truly fascinating electronic phases, such as nontrivial topological matter [2,3], chiral superconductivity [4,5], bond and charge ordering [6,7], or complex intertwined order [8,9].

In this regard the kagome materials AV_3Sb_5 (A = K, Rb, Cs) have become particularly famous, generating a real surge of research into their electronic properties [9–16]. One reason for the large interest certainly is the appearance of superconductivity in a topological Z_2 kagome metal [10]. Superconductivity in layered kagome materials is very rare to start with. But the coexistence of superconductivity and nontrivial electronic topology may support elusive and highly sought after quasiparticles such as Majorana bound states [16]. In addition to this, intriguing electronic ordering instabilities have been observed in AV_3Sb_5. Recent scanning tunneling microscopy (STM) studies, for instance, revealed the presence of electronic orders on the surfaces of KV_3Sb_5 and CsV_3Sb_5 [9,13,14].

Focusing on CsV_3Sb_5, electronic order sets in below 95 K [10,14], resulting a 2×2 superstructure, which in fact shows signatures of chirality [14]. The latter are indeed in agreement with previous theoretical studies of the kagome Hubbard model, where such an instability has been predicted [5,7]. While the formation of electronic order within the kagome layer is by now quite well established, the microscopic ordering pattern could not yet be determined. Another important feature of the electronic order in CsV_3Sb_5 is its three-dimensional (3D) character, i.e., the correlations between the kagome layers [12,16,17]. Also, these correlations remain controversial: While some studies find clear indications for a $2\times2\times2$ order [16,17], recent x-ray diffraction (XRD) studies found a disordered $2\times2\times4$ modulation [12] or even a coexistence of $2\times2\times2$ and $2\times2\times4$ superstructures [18].

Here, we study the 3D electronic order in the bulk of CsV_3Sb_5 single crystals using high-resolution XRD as a function of temperature and applied magnetic field. The basic lattice structure of this compound is illustrated in Figs. 1(a), 1(b). We show that, besides the electronic order-disorder transition at about 95 K, there is an additional order-order transition at 60 K. This order-order transition coincides with previously reported anomalies in the magnetotransport [15,19], indicating that the changes in the electronic order play a decisive role for the topological band structure of CsV_3Sb_5.

II. EXPERIMENTAL DETAILS

The zero-field measurements were done using a high-performance laboratory XRD facility, optimized for resolution and sensitivity. This custom-made instrument is equipped with a monochromatized Mo $K\beta$ radiation source (beam

*jochen.geck@tu-dresden.de

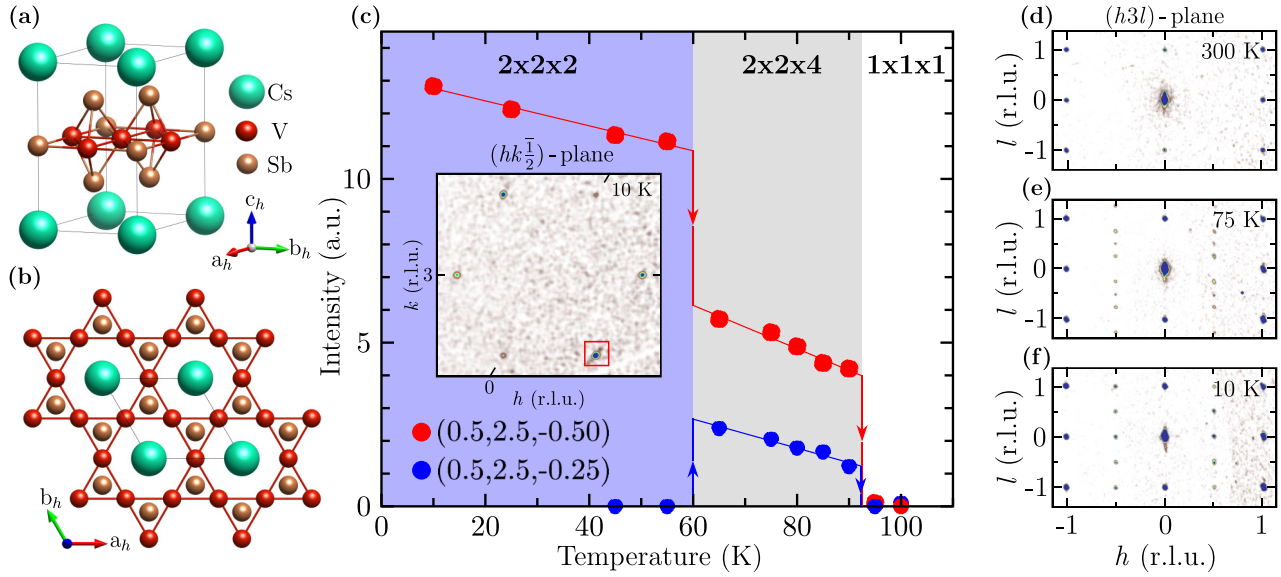

FIG. 1. Temperature-dependent XRD measurements and illustration of the three-dimensional room-temperature $P6/mmm$ structure of CsV_3Sb_5. The latter is shown in (a) together with the kagome V sublattice of a V_3Sb_5 layer in (b). The XRD data in (c)–(f) reveal the appearance of two distinct 3D superlattice modulations with different out-of-plane correlations along c_h. Data were taken with increasing temperature. (c) Temperature-dependent integrated intensity of the $(0.5, 2.5, -0.5)$ and $(0.5, 2.5, -0.25)$ superstructure reflections, which signal the presence of a $2\times2\times2$ and a $2\times2\times4$ superlattice, respectively. The red and blue lines serve as guides to the eye. Inset: Reciprocal space map parallel to the $(hk\frac{1}{2})$ plane for the $2\times2\times2$ phase at 10 K. The chirality of the XRD intensity is similar to that observed by STM [14]. $(h3l)$ planes for the undistorted $1\times1\times1$ host phase (d) at 300 K, the $2\times2\times4$ phase (e) at 75 K, and the $2\times2\times2$ phase (f) at 10 K.

diameter 70 μm on the sample) and a CdTe area detector with 300 000 pixels and no readout noise for high detection efficiency and minimum background. The outstanding performance of the instrument is particularly well demonstrated in Fig. 2(d) where peak profiles with a maximum intensity of 2 counts/s are still fully resolved. The cooling of the sample down to 10 K was accomplished by a low-vibration pulse-tube cryostat, which was itself mounted on a specialized four-circle diffractometer. High-energy (100 keV) XRD measurements in fields up to 10 T were performed at beamline P21.1 of the PETRA III storage ring (DESY, Hamburg, Germany). To apply magnetic fields along c_h and to reach temperatures down to 10 K, the CsV_3Sb_5 single crystal was mounted into a cryomagnet cooled by liquid He. The scattered radiation was again be detected using a CdTe area detector, this time with 100 000 pixels.

The single crystals for the present XRD study were synthesized using the self-flux method and well characterized prior to the XRD experiments. The magnetothermal transport measurements reveal the high quality of our CsV_3Sb_5 single crystals and show a large anomalous Nernst effect. Both the Nernst and Seebeck signals exhibit quantum oscillations, which start around 2 T [20]. The diffraction patterns at room temperature exhibit sharp and resolution-limited diffraction spots that can be indexed by a hexagonal unit cell with lattice parameters $a_h = b_h = 5.5160(14)$ Å and $c_h = 9.28(3)$ Å, again verifying the extremely high quality of the studied single crystals. In total, 145 Bragg reflections could be reached through the windows of the cryostat, 47 of them being unique. Refinement of the measured intensities [21] yielded the expected $P6/mmm$ structure and $z_{Sb_2} = 0.7422(1)$ as a single atomic coordinate not fixed by a special position, which is in perfect agreement with previously published data [22]. Throughout the following text, the Miller indices (h, k, l) of the observed diffraction peaks refer to the undistorted $1\times1\times1$ host phase with space group $P6/mmm$.

III. RESULTS

A. Zero-field measurements

Starting from room temperature, the sample was cooled down very carefully to 10 K at a rate of about 2 K per minute. After cooling down, a large number of additional superlattice reflections was observed at 10 K. The inset of Fig. 1(c), Fig. 1(f), and Figs. 2(a)–2(c) show representative reciprocal space maps and scans with typical superlattice peaks. The superlattice reflections at 10 K can be indexed referring to a unit cell, which is doubled along a_h, b_h, and c_h. We will refer to this as a $2\times2\times2$ superlattice in the following. The superlattice reflections are extremely narrow and resolution limited [full width at half maximum (FWHM) $\simeq 0.04$ reciprocal lattice units (r.l.u.)] in all three directions of reciprocal space, i.e., the bulk exhibits a fully developed 3D electronic order.

We note here that the electronic order at the surface is unstable and transforms into a stripelike 4×1 surface modulation at low temperatures [9]. The earlier attribution of this instability to surface effects [14] is in fact supported by the absence of corresponding superlattice peaks in our bulk sensitive XRD.

The main result of the present study concerns the temperature evolution of the superlattice, which is displayed in Fig. 1(c): Upon warming, the average intensity of the $2\times2\times2$ reflections decreases continuously up to about 55 K and then

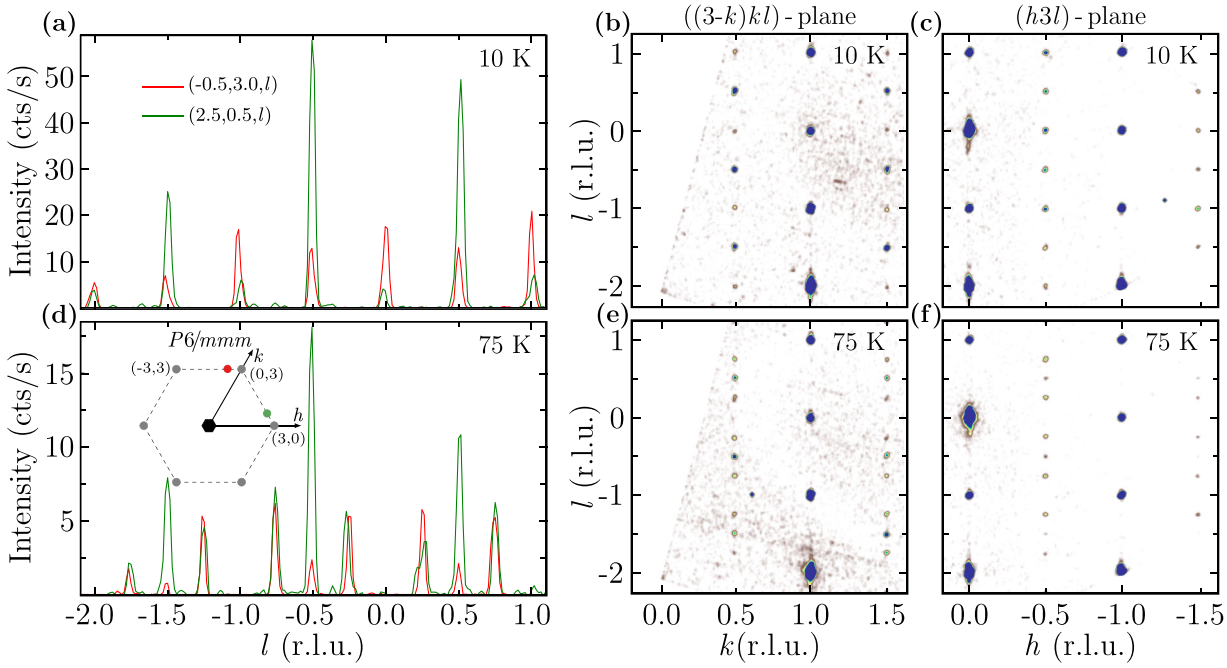

FIG. 2. Breaking of the sixfold rotational symmetry due to electronic order in the 2×2×2 and 2×2×4 phase. (a), (d) l cuts $(-0.5, 3.0, l)$ and $(2.5, 0.5, l)$, which are related by sixfold symmetry, differ in both phases (integration thickness $\delta h = \delta k = 0.06$ r.l.u.). Also the intensity distributions in reciprocal lattice planes related by sixfold symmetry are distinct as demonstrated in (b), (c) for the 2×2×2 phase and in (e), (f) for the 2×2×4. In the 2×2×4 phase the peak intensities for $l = 0.25$ still possess the sixfold rotation symmetry, while the ones with $l = 0.5$ do not (d). In the 2×2×2 phase sixfold rotation symmetry of the XRD pattern is completely lost (a). Inset: Schematic, indicating the hk positions of the measurements in (a), (d).

drops abruptly at about 60 K. Just above 60 K we observe additional peaks at positions revealing a quadrupling along the c_h direction of the $P6/mmm$ unit cell. This signals the formation of a 2×2×4 superlattice in the sense introduced above. Note that only the period of the modulation along c_h is changed, while the periodicity of the superlattice along a_h and b_h remains unaltered. The superlattice peaks of the 2×2×4 phase are also resolution limited, which can be observed in Figs. 1(e) and 2(d)–2(f). The 2×2×4 modulation therefore as well is long-ranged ordered in all three directions of space. With further increasing temperature, the decrease of the peak intensities continues, followed by an abrupt drop to zero intensity at about 95 K.

We point out that our data exclude a coexistence of the 2×2×2 and 2×2×4 phase at the measured temperatures between 60 and 95 K: The intensity of the superlattice peaks with $l = 0$ is always finite in the 2×2×2 phase, whereas it vanishes completely in the 2×2×4 phase, which is incompatible with a phase coexistence. In addition, the intensities of the superlattice peaks with $l = 0.5$ and $l = 0.25$ above 60 K exhibit a very similar temperature dependence, as can be seen in Fig. 1(c), further supporting the conclusion that all superlattice peaks have the same origin, namely the 2×2×4 phase.

The doubling along the a_h and b_h directions observed in our XRD measurements is in perfect agreement with the 2×2 superstructures detected at the surface by STM. This agreement also provides compelling evidence for the direct relation between the structural modulations probed by XRD and electronic order in the V_3Sb_5 layers probed by STM. We therefore conclude that also the structural transition at 60 K reflects a change in the electronic order. More specifically, the superlattice reflections reveal a reoganization of electronically ordered kagome layers along c_h, while the periodicity of the electronic order in the $a_h b_h$ plane remains unchanged.

It is important to note that a previous XRD study reported a 2×2×4 phase at 15 K [12], instead of the 2×2×2 phase observed here. Furthermore, another very recent XRD study found a coexistence of the 2×2×2 and 2×2×4 phases below 95 K, which depends on the cooling protocol [18]. In both studies, the XRD intensity maps show broad streaks along the reciprocal l direction due to considerable disorder along the c_h direction. These results therefore imply that the 2×2×2 and 2×2×4 phases are close in energy and metastable under certain conditions.

We argue that the present XRD results correspond to intrinsic electronic order in thermal equilibrium: First, the superlattices observed here are highly ordered in all three dimensions, which is a very strong indication that these structures belong to the thermodynamically stable phase. We also find the electronic order to be phase pure, i.e., there is no coexistence of different types of electronic order. Second, the observed transition temperatures agree perfectly with a number of previous reports: The transition at $T_{c1} = 95$ K is fully consistent with anomalies observed in the magnetic susceptibility, electrical resistivity, and the specific heat [10,14]. But more importantly, the transition at $T_{c2} = 60$ K is in perfect agreement with previous magnetotransport studies where precisely at this temperature striking anomalies were observed [15,19]. It also corresponds very closely to a drastic change in the temperature-dependent Seebeck coefficient [20]. The

rearrangement of the electronic order at T_{c2} is therefore directly related to changes in the macroscopic properties.

In Figs. 2(a) and 2(d), l cuts at two hk positions, which are equivalent in $P6/mmm$, are shown. Clearly, the l cuts at the two positions differ, showing that the sixfold symmetry of $P6/mmm$ is indeed broken by the electronic order in both the $2\times2\times2$ and $2\times2\times4$ phases. This can also be observed very nicely in Figs. 2(b) and 2(c) and Figs. 2(e) and 2(f), which compare the intensity distributions in reciprocal lattice planes related by the sixfold symmetry. Our data therefore exclude high-symmetry charge ordering models with $P6/mmm$ symmetry discussed in the literature [23].

B. Magnetic field-dependent measurements

Now we turn to another very striking feature of the XRD intensity distribution, namely its chirality. As can be observed in the inset of Fig. 1(c), the intensities exhibit a chirality in the (hk) plane very similar to what has been observed by STM [13,14]. These STM studies also revealed that the chirality of the electronic order at the surface can be altered by a magnetic field of 2 T applied along the c_h direction. The chirality detected in STM hence appears to be linked to time-reversal symmetry breaking (TRS breaking). Indeed, chiral electronic order yielding time-reversal symmetry is found in the kagome Hubbard model, where it results from sublattice interference within a single kagome plane [5,7]. Interestingly, a very recent muon spin rotation (μSR) study of KV_3Sb_5 reports the evidence for time-reversal symmetry breaking due to electronic order [24]. These μSR data also show additional anomalies at lower temperature, which may correspond to the transition at $T_{c2} = 60$ K.

But when interpreting the chiral XRD pattern from a bulk sample care must be taken: Twinning of a nonchiral superstructure, for example, can also yield a chiral XRD intensity distribution. The chirality of the XRD intensities presented in the inset of Fig. 1(c) can therefore not be taken as proof for chiral electronic order.

In order to further investigate possible sample twinning and TRS breaking in CsV_3Sb_5, we performed XRD with 100 keV synchrotron radiation in applied magnetic fields up to 10 T. The use of synchrotron radiation provides an even higher q resolution than the zero-field measurements performed in house. As in the STM studies mentioned above, the magnetic field was applied parallel to the c_h axis.

The sample was first cooled down into the $2\times2\times2$ phase in zero magnetic field. As can be seen in Fig. 3, within the error of the present measurement, no change of the peak profiles was observed upon increasing the magnetic field to 10 T. We also applied -10 T and performed field-cooled measurements. In all cases, the peak position and width remained unchanged and also the intensity remained constant within about 5%, which corresponds to the experimental error of the setup. Slight variations in the profiles can be attributed to small changes of the sample position of the order of ±10 μm. Instead, the high q resolution of the present synchrotron experiment revealed small peak splittings due to the twinning of our single crystal (see inset of Fig. 3). We therefore conclude that the chiral XRD pattern detected in the present experiment is, first, indeed caused by a twinning of the sample and, second, not related to TRS breaking. Our results can hence neither prove nor disprove chiral electronic ordering or TRS breaking in CsV_3Sb_5.

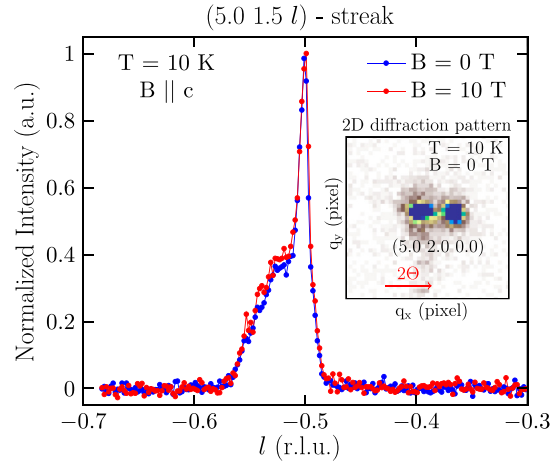

FIG. 3. Magnetic field-dependent XRD measurements. Blue curve: (5.0, 1.5, −0.5) peak of the $2\times2\times2$ phase in the zero-field cooled state at 10 K and 0 T. The structure of the intensity profile is due to the mosaic of the sample. As the magnetic field along the c_h direction is increased from 0 to 10 T, the intensity of the (5.0, 1.5, −0.5) superstructure peak remains unchanged (red curve). Inset: A two-dimensional detector image showing twin-induced peak splitting at the (5.0,2.0,0.0) position. Increasing q_x corresponds to an increasing scattering angle 2Θ.

C. Crystallographic refinements

While the twinning of the superstructure, combined with the small intensity of the superlattice peaks, currently prevents a detailed crystallographic analysis of the $2\times2\times4$ phase, we succeeded in analyzing the zero-field data sets for the $2\times2\times2$ phase at low temperatures. A key factor here was the unmatched quality of the present XRD data from a phase-pure $2\times2\times2$ phase. The crystallographic refinements of the $2\times2\times2$ superlattice were performed in the space group $Fmmm$, which was also found in previous theoretical investigations [23]. While the base-centered orthorhombic $Cmcm$, which corresponds to one of the structures proposed in Ref. [25], can be excluded based on reflection conditions, we also considered a monoclinic distortion to $C2/m$. However, both $Fmmm$ and $C2/m$ yield essentially the same atomic positions in direct space, i.e., we cannot discriminate between these two space groups based on the present data. Since our data do not show signs of a significant monoclinic distortion, we use the higher symmetric $Fmmm$ in the following.

Our analysis showed that the measured XRD data are very well reproduced by two different superlattices, namely a staggered star-of-David (SOD) and staggered inverse SOD shown in Fig. 4 (structural parameters can be found in the Appendix). Our results are in fact perfectly in line with other recent studies [17,18,25].

The two solutions found in the crystallographic refinements mainly differ in the sign of the displacement vectors, which describe the shifts of the V sites in the $2\times2\times2$ phase

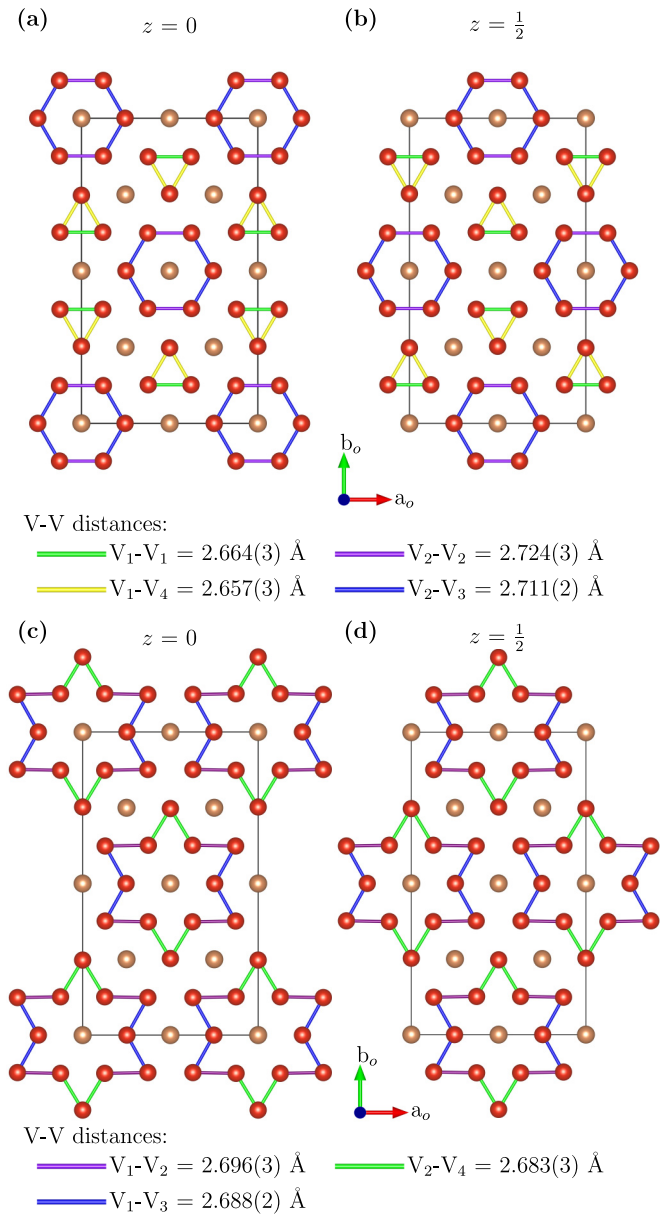

FIG. 4. Illustration of the refined structural models for the 2×2×2 phase at low temperatures. Model 1 (staggered inverse SOD) in (a), (b) and model 2 (staggered SOD) in (c), (d). The two planes at $z = 0$ and $z = 0.5$ alternate along the c direction (out of plane), which results in a staggered ordering. The different nearest-neighbor V-V distances are encoded by different colors, as indicated below the corresponding panels.

with respect to an unmodulated structure. This ambiguity of the present analysis stems from the twinning of the superlattice in combination with the relatively small intensities of the superlattice peaks.

IV. CONCLUSION

To conclude, we studied the 3D bulk electronic order in CsV_3Sb_5 and obtained two main results: First, an order-order transition at 60 K, which involves a change of the correlations between kagome layers and anomalies in the magnetotransport. Second, we performed a crystallographic refinement of the 2×2×2 phase and found two possible solutions, namely a staggered SOD and a staggered inverse SOD. While we cannot determine which of the two solutions corresponds to the 2×2×2 phase of CsV_3Sb_5, this experimentally determined structural information will enable us to test, assess, and improve available theoretical models.

The reorganization at 60 K implies that different ordering patterns are energetically very close, which is also highlighted by the fact that more surface sensitive methods found uniaxial order [9] or a coexistence of inverse SOD and SOD type order [26]. All this indicates highly tunable ordering instabilities that in particular may depend on the number of layers in few layer systems. This still needs to be explored systematically. It also remains to be clarified whether or under which conditions chiral charge order or possible nematic instabilities occur in AV_3Sb_5. These open issues certainly deserve further study and will very likely yield more surprises in the future.

ACKNOWLEDGMENTS

This research has been supported by the Deutsche Forschungsgemeinschaft through SFB 1143 (project-id 247310070), the Würzburg-Dresden Cluster of Excellence on Complexity and Topology in Quantum Matter–ct.qmat (EXC 2147, project-id 390858490), and SFB 1415 (project-id 417590517). C.F., D.C., and C.S. also gratefully acknowledge additional support by the European Research Council Advanced Grant (No. 742068) "TOPMAT" and the Deutsche Forschungsgemeinschaft (project-id 258499086). We acknowledge DESY (Hamburg, Germany), a member of the Helmholtz Association HGF, for the provision of experimental facilities. Parts of this research were carried out at beamline P21.1 at PETRA III.

APPENDIX: CRYSTALLOGRAPHIC REFINEMENTS

For data processing information, see Ref. [21]. As described in the main text, we obtained two models, which

TABLE I. Refined atomic coordinates and equivalent isotropic displacement parameters for the staggered inverse star-of-David superstructure (model 1), as shown in Figs. 4(a) and 4(b).

Atom	Site	x	y	z	U_{eq}
Cs_1	8*i*	0	0	0.75074(8)	0.0086(9)
Cs_2	8*f*	0.25	0.25	0.25	0.0085(9)
V_1	16*o*	0.37859(12)	0.12630(6)	0	0.0068(10)
V_2	16*o*	0.62415(12)	0.37624(6)	0	0.0066(10)
V_3	8*g*	0.2475(2)	0	0	0.0091(14)
V_4	8*h*	0	0.74741(10)	0	0.0088(14)
Sb_1	16*m*	0	0.33294(5)	0.62156(10)	0.0072(9)
Sb_2	32*p*	0.25056(3)	0.08348(4)	0.12162(9)	0.0072(9)
Sb_3	16*m*	0	0.83339(5)	0.62338(10)	0.0072(9)
Sb_4	4*b*	0	0	0.5	0.0073(10)
Sb_5	8*e*	0.25	0.25	0	0.0074(10)
Sb_6	4*a*	0	0	0	0.0075(10)

TABLE II. Refined atomic coordinates and equivalent isotropic displacement parameters for the staggered star-of-David superstructure (model 2), as shown in Figs. 4(c) and 4(d).

Atom	Site	x	y	z	U_{eq}
Cs_1	8*i*	0	0	0.74923(9)	0.0086(9)
Cs_2	8*f*	0.25	0.25	0.25	0.0087(9)
V_1	16*o*	0.37154(13)	0.12373(7)	0	0.0059(10)
V_2	16*o*	0.62587(14)	0.37374(7)	0	0.0076(11)
V_3	8*g*	0.2525(2)	0	0	0.0099(15)
V_4	8*h*	0	0.75259(12)	0	0.0081(15)
Sb_1	16*m*	0	0.33369(5)	0.62251(10)	0.0073(9)
Sb_2	32*p*	0.24944(4)	0.08317(5)	0.12247(9)	0.0073(9)
Sb_3	16*m*	0	0.83327(5)	0.62070(11)	0.0073(9)
Sb_4	4*b*	0	0	0.5	0.0075(10)
Sb_5	8*e*	0.25	0.25	0	0.0075(10)
Sb_6	4*a*	0	0	0	0.0077(10)

describe the data equally well, namely the inverse SOD (model 1) and the SOD (model 2). Both models feature a staggered ordering along the c_o axis. The main difference is an inversion of the positional shift of the V sites. Details about the refinements and the data sets are provided in Tables I–III.

TABLE III. Details on data collection and structure. Top: Parameters characterizing the data collection and the crystal structure. Bottom: Comparison of the refinements of model 1 and model 2. Both models describe the experimental data equally well, with a slightly better fit by model 1.

Crystal data		Data collection	
Temperature (K)	10	Wavelength (Å)	0.63229
Crystal system	Orthorhombic	$2\theta_{max}$ (deg)	45.36
Space group	*Fmmm*	$N_{measured}$	914
a (Å)	10.9713(14)	$N_{independent}$	474
b (Å)	18.983(3)	$N_{observed}$ $[I > 2\sigma(I)]$	292
c (Å)	18.514(10)	μ (mm^{-1})	13.76
Z	16	R_{int} (%)	6.52
ρ_{calc} (g cm^{-3})	6.163		
Refinement	**Model 1**		**Model 2**
$N_{parameters}$	30		30
$R_1 > 4\sigma$ (%)	3.17		3.37
R_1 all (%)	3.91		4.12
$wR_2 > 4\sigma$ (%)	13.07		13.97
wR_2 all (%)	15.51		16.16
Extinction	0.00013		0.00013
Twin fractions	65 : 16 : 19		65 : 16 : 19
Goodness of fit	1.133		1.102
$\Delta\rho_{min}$ (e Å^{-3})	−1.234		−1.231
$\Delta\rho_{max}$ (e Å^{-3})	1.033		1.024

[1] S. Sachdev, Phys. Rev. B **45**, 12377 (1992).
[2] H.-M. Guo and M. Franz, Phys. Rev. B **80**, 113102 (2009).
[3] T. Bilitewski and R. Moessner, Phys. Rev. B **98**, 235109 (2018).
[4] S.-L. Yu and J.-X. Li, Phys. Rev. B **85**, 144402 (2012).
[5] M. L. Kiesel and R. Thomale, Phys. Rev. B **86**, 121105(R) (2012).
[6] W.-S. Wang, Z.-Z. Li, Y.-Y. Xiang, and Q.-H. Wang, Phys. Rev. B **87**, 115135 (2013).
[7] M. L. Kiesel, C. Platt, and R. Thomale, Phys. Rev. Lett. **110**, 126405 (2013).
[8] F. H. Yu, D. H. Ma, W. Z. Zhuo, S. Q. Liu, X. K. Wen, B. Lei, J. J. Ying, and X. H. Chen, Nat. Commun. **12**, 3645 (2021).
[9] H. Zhao, H. Li, B. R. Ortiz, S. M. L. Teicher, T. Park, M. Ye, Z. Wang, L. Balents, S. D. Wilson, and I. Zeljkovic, Nature (London) **599**, 216 (2021).
[10] B. R. Ortiz, S. M. L. Teicher, Y. Hu, J. L. Zuo, P. M. Sarte, E. C. Schueller, A. M. M. Abeykoon, M. J. Krogstad, S. Rosenkranz, R. Osborn, R. Seshadri, L. Balents, J. He, and S. D. Wilson, Phys. Rev. Lett. **125**, 247002 (2020).
[11] M. M. Denner, R. Thomale, and T. Neupert, Phys. Rev. Lett. **127**, 217601 (2021).
[12] B. R. Ortiz, S. M. L. Teicher, L. Kautzsch, P. M. Sarte, N. Ratcliff, J. Harter, J. P. C. Ruff, R. Seshadri, and S. D. Wilson, Phys. Rev. X **11**, 041030 (2021).
[13] Y.-X. Jiang, J.-X. Yin, M. M. Denner, N. Shumiya, B. R. Ortiz, G. Xu, Z. Guguchia, J. He, M. S. Hossain, X. Liu, J. Ruff, L. Kautzsch, S. S. Zhang, G. Chang, I. Belopolski, Q. Zhang, T. A. Cochran, D. Multer, M. Litskevich, Z.-J. Cheng *et al.*, Nat. Mater. **20**, 1353 (2021).
[14] Z. Wang, Y.-X. Jiang, J.-X. Yin, Y. Li, G.-Y. Wang, H.-L. Huang, S. Shao, J. Liu, P. Zhu, N. Shumiya, M. S. Hossain, H. Liu, Y. Shi, J. Duan, X. Li, G. Chang, P. Dai, Z. Ye, G. Xu, Y. Wang *et al.*, Phys. Rev. B **104**, 075148 (2021).
[15] H. Chen, H. Yang, B. Hu, Z. Zhao, J. Yuan, Y. Xing, G. Qian, Z. Huang, G. Li, Y. Ye, S. Ma, S. Ni, H. Zhang, Q. Yin, C. Gong, Z. Tu, H. Lei, H. Tan, S. Zhou, C. Shen *et al.*, Nature (London) **599**, 222 (2021).
[16] Z. Liang, X. Hou, F. Zhang, W. Ma, P. Wu, Z. Zhang, F. Yu, J. J. Ying, K. Jiang, L. Shan, Z. Wang, and X. H. Chen, Phys. Rev. X **11**, 031026 (2021).
[17] N. Ratcliff, L. Hallett, B. R. Ortiz, S. D. Wilson, and J. W. Harter, Phys. Rev. Materials **5**, L111801 (2021).
[18] Q. Xiao, Y. Lin, Q. Li, W. Xia, X. Zheng, S. Zhang, Y. Guo, J. Feng, and Y. Peng, arXiv:2201.05211.
[19] Y. Xiang, Q. Li, Y. Li, W. Xie, H. Yang, Z. Wang, Y. Yao, and H.-H. Wen, Nat. Commun. **12**, 6727 (2021).
[20] D. Chen, B. He, M. Yao, Y. Pan, H. Lin, W. Schnelle, Y. Sun, J. Gooth, L. Taillefer, and C. Felser, Phys. Rev. B **105**, L201109 (2022).
[21] Data processing was performed in the CRYSALISPRO software suite (version 171.41.93a) [27]. Corrections based on the multiscan method were applied using the SCALE3 ABSPACK scaling algorithm. The subsequent structure solution and weighted full-matrix least-squares refinement on F^2 were done with SHELXT-2014/5 [28] and SHELXL-2018/3 [29] as implemented in the WINGX 2018.3 program suite [30].
[22] B. R. Ortiz, L. C. Gomes, J. R. Morey, M. Winiarski, M. Bordelon, J. S. Mangum, I. W. H. Oswald, J. A. Rodriguez-

Rivera, J. R. Neilson, S. D. Wilson, E. Ertekin, T. M. McQueen, and E. S. Toberer, Phys. Rev. Materials **3**, 094407 (2019).

[23] M. H. Christensen, T. Birol, B. M. Andersen, and R. M. Fernandes, Phys. Rev. B **104**, 214513 (2021).

[24] C. Mielke, D. Das, J.-X. Yin, H. Liu, R. Gupta, Y.-X. Jiang, M. Medarde, X. Wu, H. C. Lei, J. Chang, P. Dai, Q. Si, H. Miao, R. Thomale, T. Neupert, Y. Shi, R. Khasanov, M. Z. Hasan, H. Luetkens, and Z. Guguchia, Nature (London) **602**, 245 (2022).

[25] A. Subedi, Phys. Rev. Materials **6**, 015001 (2022).

[26] Y. Hu, X. Wu, B. R. Ortiz, X. Han, N. C. Plumb, S. D. Wilson, A. P. Schnyder, and M. Shi, arXiv:2201.06477.

[27] Rigaku Oxford Diffraction, CrysAlisPro Software system version 1.171.39.46, Rigaku Corporation, Oxford, 2018.

[28] G. M. Sheldrick, Acta Cryst. A **71**, 3 (2015).

[29] G. M. Sheldrick, Acta Cryst. C **71**, 3 (2015).

[30] L. J. Farrugia, J. Appl. Cryst. **45**, 849 (2012).